Partitioning of Ozone Loss Pathways in the Ozone Quasi-biennial Oscillation Simulated by a Chemistry-Climate Model

Kiyotaka SHIBATA

Kochi University of Technology, Kochi, Japan
Meteorological Research Institute, Tsukuba, Japan

and

Ralph LEHMANN

Alfred Wegener Institute, Helmholtz Centre for Polar and Marine Research, Germany

Abstract

Ozone loss pathways and their rates in the ozone quasi-biennial oscillation (QBO), which is simulated by a chemistry-climate model developed by the Meteorological Research Institute of Japan, are evaluated using an objective pathway analysis program (PAP). The analyzed chemical system contains catalytic cycles caused by NO_x, HO_x, ClO_x, O_x, and BrO_x. PAP quantified the rates of all significant catalytic ozone loss cycles, and evaluated the partitioning among these cycles. The QBO amplitude of the sum of all cycles amounts to about 4 and 14 % of the annual mean of the total ozone loss rate at 10 and 20 hPa, respectively. The contribution of catalytic cycles to the QBO of the ozone loss rate is found to be as follows: NO_x cycles contribute the largest fraction (50−85 %) of the QBO amplitude of the total ozone loss rate; HO_x cycles are the second-largest (20−30 %) below 30 hPa and the third-largest (about 10 %) above 20 hPa; O_x cycles rank third (5−20 %) below 30 hPa and second (about 20 %) above 20 hPa; ClO_x cycles rank fourth (5−10 %); and BrO_x cycles are almost negligible. The relative contribution of the NO_x and O_x cycles to the QBO amplitude of ozone loss differs by up to 10 % and 20 %, respectively, from their contribution to the annual mean ozone loss rate. The ozone QBO at 20 hPa is mainly driven by ozone transport, which then alters the ozone loss rate. In contrast, the ozone QBO at 10 hPa is driven chemically by NO_x and the temperature dependence of $[O]/[O_3]$, which results from the temperature dependence of the reaction $O + O_2 + M \rightarrow O_3 + M$. In addition, the ozone QBO at 10 hPa is influenced by the overhead ozone column, which affects $[O]/[O_3]$ (through ozone photolysis) and the ozone production rate (through oxygen photolysis).

Corresponding author: Kiyotaka Shibata, School of Environmental Science and Engineering Kochi University of Technology, 185 Miyanokuchi, Tosayamada, Kami, Kochi 782-8502, Japan
E-mail: shibata.kiyotaka@kochi-tech.ac.jp
J-stage Advance Published Date: 2 April 2020

1. Introduction

The quasi-biennial oscillation (QBO) in zonal wind and temperature is one of the largest variations in the equatorial stratosphere, and its effects can reach the extratropics as far as the North Pole (e.g., Baldwin et al. 2001). Together with the QBO in dynamical quantities, trace gases like ozone show similar oscillations in the equatorial stratosphere due to the transport and/or chemistry associated with the QBO, and the corresponding ozone oscillation is thereby called the ozone QBO. Detailed vertical and temporal structures of the QBO in O_3 and NO_2 were revealed through Stratospheric Aerosol and Gas Experiment (SAGE) II data by Zawodny and McCormick (1991), Hasebe (1994), and Chipperfield et al. (1994) and through Global Ozone Monitoring by Occultation of Stars (GOMOS) data by Hauchecorne et al. (2010) and Liu et al. (2011). By analyzing the Optical Spectrograph and Infrared Imager System data, Park et al. (2017) have also showed the detailed structures of the QBO in O_3, NO_x, N_2O, and HNO_3. Unlike the zonal wind, temperature, and NO_2, these studies demonstrated that the ozone QBO has a distinctly sharp phase change (transition) at around 28 km, where the transition occurs between dynamical control below and photochemical control above. The ozone and temperature signals are in phase below the transition altitude, while they are out of phase above it.

The ozone QBO in the dynamically controlled region is interpreted as being driven by transport due to vertical motion, which is a part of the secondary circulation of the QBO (Plumb and Bell 1982). On the other hand, the cause of the ozone QBO in the photochemically controlled region has not yet been fully determined. The sharp phase change in the ozone QBO has been investigated with numerical models. Ling and London (1986), using a one-dimensional model, attributed the ozone QBO in the photochemically controlled region as the effect of temperature on the rate constants for reactions of ozone destruction. On the other hand, Chipperfield et al. (1994) asserted that Ling and London (1986) have disregarded the feedback of the NO_2 variations on the ozone by using a fixed NO_2 profile, and he further demonstrated, using a two-dimensional model, that the ozone QBO above the transition altitude is due primarily to the $NO–NO_2$ catalytic cycles of ozone destruction. Tian et al. (2006), using of a fully coupled chemistry-climate model (CCM) and a photochemical box model, confirmed that NO_x is the main chemical driver of the ozone QBO above the transition altitude.

However, using a three-dimensional chemistry transport model without QBO-induced variations in odd nitrogen (NO_y) transport, Butchart et al. (2003) reproduced the ozone QBO with a phase reversal (relative to the phase of the QBO of the horizontal wind) near 10 hPa and an amplitude consistent with observations. The intermediate importance of NO_x was detected by Fleming et al. (2002), who found that the QBO in odd nitrogen radicals plays a significant but not dominant role in determining the ozone QBO.

There exist many catalytic cycles of ozone destruction, and the dominant ones vary from one situation to another, depending on conditions such as temperature, solar zenith angle, altitude, and concentrations of ambient trace gases including ozone and aerosols. Moreover, the analysis of catalytic cycles is primarily based on a predefined set of cycles, which is not necessarily the same in different studies (e.g., Wennberg et al. 1994; Jucks et al. 1996; Nevison et al. 1999). Quantifying the contribution of each catalytic ozone destruction cycles is not straightforwardly performed, as different cycles may share some reactions, which makes the calculation of rates of cycles difficult. A quantitative evaluation of stratospheric ozone chemistry without the explicit specification of full catalytic cycles was made, e.g., by Osterman et al. (1997) and Meul et al. (2014). They evaluated the rate-limiting reactions, but did not aim at the ozone QBO. Osterman et al. (1997) calculated the daily mean O_x production and loss rates by reactions involving different families of chemical species (NO_x, HO_x, ClO_x, O_x, and BrO_x) with a photochemical model, based on balloon observed data in the stratosphere at 34.5°N, 104.2°W in September 1993. Meul et al. (2014) quantified the ozone production and loss cycles in the tropical stratosphere under the current climate and for a projected climate at the end of the twenty-first century by performing an off-line evaluation of chemical reactions, in which 6-hourly CCM output for the temperature and a set of chemical constituents were used.

In this study, we use the pathway analysis program (PAP), developed by Lehmann (2002, 2004), to quantify the partitioning of catalytic ozone destruction cycles in the equatorial stratosphere. This program can objectively determine and evaluate (= assign a rate to) all significant pathways in chemical reaction systems. So far, PAP has been utilized for various analyses such as:

- Stratospheric and mesospheric ozone (Grenfell et al. 2006)
- Chlorine chemistry in the Antarctic lower stratosphere (Müller et al. 2018)

- Mesospheric nitric acid enhancements and ionic reactions affecting middle atmospheric HO_x and NO_y during solar proton events (Verronen et al. 2011; Verronen and Lehmann 2013)
- CO_2 and ozone in the Martian atmosphere (Stock et al. 2012a, b; Stock et al. 2017)
- Photochemical reactions in super-Earth atmospheres (Grenfell et al. 2013)

This study aims to quantify the partitioning of ozone loss pathways caused by the following: nitrogen oxides ($NO_x = NO + NO_2 + NO_3$), odd hydrogen ($HO_x = H + OH + HO_2$), reactive chlorine ($ClO_x = Cl + ClO + 2 \times Cl_2O_2$), odd oxygen ($O_x = O_3 + O(^3P) + O(^1D)$), and reactive bromine ($BrO_x = Br + BrO$) cycles in the ozone QBO simulated by the CCM of the Meteorological Research Institute (MRI) of Japan (MRI-CCM). The dynamical features of the QBO simulated by MRI-CCM were investigated in detail by comparing them with those of the observed QBO (e.g., Shibata and Deushi 2008b; Naoe and Shibata 2010). The rest of this paper is arranged as follows. Section 2 describes the model, simulation conditions, and the chemical pathway analysis done by PAP. Section 3 presents the simulated QBO in dynamics and chemistry. Section 4 describes the partitioning of ozone loss cycles in the QBO as well as that in the annual mean. The mechanism of the generation of the ozone QBO is investigated in more detail in Section 5, and lastly, conclusions are presented in Section 6.

2. Method

2.1 Chemistry-climate model

The MRI-CCM used in this study is nearly identical to the one used in previous studies (Shibata and Deushi 2008a, 2012), except for its increased number of vertical layers (81 instead of 68) to improve the vertical resolution in the upper stratosphere and mesosphere (above 10 hPa). The 81- and 68-layer CCMs are indicated as L81 and L68, respectively. Details of the previous MRI-CCM are described in Shibata and Deushi (2008a), that is why only a brief description of its dynamics and chemistry is provided here. The dynamics module of MRI-CCM is a spectral global model with triangular truncation, a maximum total wavenumber 42 (T42, about 2.8° by 2.8° in longitude and latitude grid space), and 81 layers in the eta-coordinate with a lid at 0.01 hPa (about 80 km). We call this version T42L81, which generates the QBO internally, similar to the previous T42L68, as will be shown later. The vertical spacing is about 500 m in the stratosphere between 100 hPa and 10 hPa, continuously increasing downward to the level of about 200 hPa

and upward to the model lid. The above-mentioned improvement of the vertical resolution above 10 hPa resulted in a more gradual layer broadening with a layer thickness of $1 \sim 2$ km in the upper stratosphere and lower mesosphere. Non-orographic gravity-wave forcing by Hines (1997) is incorporated with an enhanced source strength of a Gaussian function equatorward of 30°. Biharmonic (Δ^2) horizontal diffusion is minimized only in the middle atmosphere compared to that in the troposphere to spontaneously reproduce the QBO in zonal wind while minimizing the changes in the troposphere (Shibata and Deushi 2005a, b). In addition, vertical diffusion is not applied in the middle atmosphere to keep the sharp vertical shear in the QBO. The chemistry-transport module employs a hybrid semi-Lagrangian transport scheme compatible with the continuity equation to satisfy the mass conservation. The chemistry scheme treats 36 long-lived species including 7 families and 15 short-lived species with 80 gas-phase reactions, 35 photochemical reactions, and 9 heterogeneous reactions on polar stratospheric clouds and sulfate aerosols. The chemistry module of MRI-CCM was an update from the previous version (Shibata and Deushi 2008a, 2012) in the following points. The typographical error of the photolysis of CFC-12 (chlorofluorocarbon-12, CCl_2F_2) in JPL02 (Sander et al. 2002) was corrected to JPL06 (Sander et al. 2006). The Sun-Earth distance effect on photolysis was incorporated. The following three OH reactions were added: $OH + OH \rightarrow H_2O + O$, $OH + OH + M \rightarrow H_2O_2 + M$, $ClO + OH \rightarrow HCl + O_2$, resulting in 83 gas-phase reactions. Nighttime chemistry was upgraded, so that it will be identical with the daytime chemistry except that photolysis rates and $O(^1D)$ are set to zero at night. As a result, the simulated stratospheric ozone decreased, mainly due to the corrected CFC-12 photolysis.

The temporal change of ozone due to transport, in Section 5.2.a, is calculated as the difference between the ozone mixing ratios after and before a transport time step of the model. Similarly, the temporal change of ozone due to chemistry is evaluated as the difference between after and before chemistry calculation. The overhead ozone column, found in Sections 5.2.b and 5.2.c, is defined at half-levels k-1/2, i.e., at the interface level between the adjacent upper layer k-1 and lower layer k. It is computed as a sum of the ozone concentration (multiplied by the layer thickness) from the top ($k = 1$) layer to the layer k-1, and hence it does not include the ozone in layer k. That is, the variations in the overhead column ozone at pressure level p do not include the variation of ozone in the layer at p.

2.2 Model simulation

The MRI-CCM of T42L81 version was integrated using an initial condition from L68 restart data on August 1 1970. It was under the CCMVal-2 B2 scenario (SPARC CCMVal 2010), i.e., REF-B2, which was made for simulations from 1960 to 2100, with a time-evolving forcing by greenhouse gases (GHGs), ozone depleting substances (ODSs), and sea surface temperature (SST) and with fixed solar minimum and background aerosol conditions in the stratosphere. The integration was performed until November 2020, referred to as a standard run (ST run). Moreover, to collect the detailed chemistry data for PAP, i.e., rates of all the chemical reactions in the system and concentrations of all the species averaged over a time interval of interest, MRI-CCM of L81 was again run for a certain period, using the restart data at the end of relevant months of the ST run. One-day (24 hours) integrations were conducted every three months, i.e., for the first days of January, April, July, and October from January 1972 to April 1990, assuming that the sampling interval of three months is short enough to reproduce the overall features of the QBO (having a period of about two years) generated in the ST run. The one-day integrations are called as pathway analysis run (PA run). As will be demonstrated later, the three-monthly 1-day mean data capture the general QBO characteristics in the ST run in spite of lacking certain temporal fine structures.

2.3 Pathway analysis program

The details of PAP are only briefly described here, as these are fully discussed by Lehmann (2002, 2004). This is an algorithm that objectively determines all the significant pathways (reaction sequences) in an arbitrary chemical system. It may be summarized as follows. The algorithm starts from individual reactions. The chemical species in the system, one after the other, are treated as so-called "branching-points". For every branching-point species, each pathway producing it is connected with each pathway consuming it. If a newly formed pathway contains sub-pathways, e.g., null cycles, it is split into these simpler pathways. Based on known reaction rates (usually from a chemical model run), the so-called "branching probabilities" are calculated and used to determine a rate for each pathway. In order to avoid a too large number of pathways ("combinational explosion"), pathways with a rate smaller than a prescribed threshold are deleted during the construction process.

One advantage of PAP when used in ozone chemistry is its accurate and objective evaluation of the rel-

evant catalytic cycles of ozone loss by excluding null cycles. For example, one of the ozone loss reactions evaluated by Bruhwiler and Hamilton (1999) is $OH + O_3 \rightarrow HO_2 + O_2$. However, this reaction is also included in the following zero cycles, $OH + O_3 \rightarrow HO_2 + O_2$, $HO_2 + NO \rightarrow OH + NO_2$, $NO_2 + hv \rightarrow NO + O$, and $O + O_2 + M \rightarrow O_3 + M$, so that a significant fraction of the rate of this reaction does not lead to ozone loss.

As stated before, PAP requires a list of all the chemical reactions in the system, concentrations of all the species averaged over a time interval of interest, and rates of all reactions integrated over the same time interval. To prepare the full data for PAP, we set 32 equally spaced grid points at 1.4°N, nearest to the equator in T42 quadratic Gaussian latitudes, with the longitudinal interval being 11.25 degrees, and stored the rate constants and concentrations of chemical species at these grids before and after each chemistry time step of the model. Then we averaged the reaction rates and concentrations of chemical species on all the grid points at 1.4°N and all the time steps over the whole integration period, i.e., 24 hours. In principle, PAP should be applied for immediate chemical reactions, i.e., for one time-step of the integration of the differential equations describing the chemical reactions, but it can also be applied for temporally averaged data (e.g., Grenfell et al. 2006).

3. Results of the simulation of the QBO

3.1 QBO of zonal wind and temperature

Figure 1 shows the power spectrum of the simulated and the observed zonal-mean zonal wind, latitudinally averaged within 10 degrees of the equator from 100 to 1 hPa. The simulated wind is taken from the ST run, in which the monthly mean data span 50 years from 1970 to 2020, while the observed wind is from the merged reanalysis data of ERA-40 (Uppala et al 2005) and ERA-Interim (Dee et al. 2011), spanning about 55 years from 1958 to 2013. There are three major modes of variability: semi-annual oscillation (SAO), annual cycle, and the QBO. The simulated QBO wind spectrum is quite similar to the observed one, with the center period being about 27 months in the simulation and 28 months in the observation, as in the previous version of the L68 MRI-CCM in the REF-B2 runs (Shibata and Deushi 2012). Although the simulated power spectrum of the QBO is similar to the observation, the observed QBO exhibits a more broadly spread spectrum, particularly in the far wing of longer periods. This is due in parts to the facts that the simulation includes neither the 11-year solar cycle nor volcanic aerosols from the three huge eruptions of
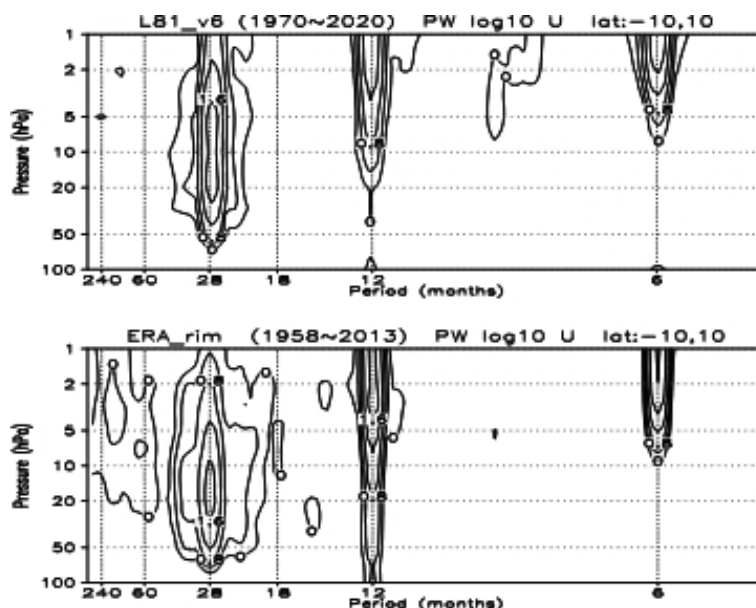
Fig. 1. Power spectrum of zonal-mean zonal wind from 100 to 1 hPa averaged between 10°S and 10°N (upper) in the ST run from 1970 to 2020 and (lower) in the merged data of ERA-40 and ERA-Interim from 1958 to 2013. Values are displayed in logarithmic scale of base 10, and units are $m^2 \, s^{-2}$. Contour interval is 0.4.

Agung, El Chichón, and Mount Pinatubo.

Figure 2 presents the anomalies of the observed (ERA-40) and the simulated zonal-mean zonal wind and temperature (averaged between 10°S and 10°N) from 70 to 5 hPa. It spanned for about 18 years from 1972 to 1990, together with the zonal-mean zonal wind anomalies at 30 hPa, in which anomalies are calculated by subtracting the mean annual cycle (averaged over all 18 years), in order to diminish the SAO, which is almost synchronized with the seasonal cycle. It should be noted that the QBO phase is different in the observation and the simulation, because the simulated QBO is spontaneously generated with an average period of about one month shorter than the observation (Fig. 1). The simulated wind evidently reproduced the overall features of the observed QBO such as the faster downward propagation of westerly shear (defined as positive wind shear $du/dz > 0$) than easterly shear ($du/dz < 0$) as manifested in the zonal wind time series at 30 hPa (Figs. 2b, d). The temperature anomaly, the phase of which is approximately advanced about one quarter cycle from that of the zonal wind anomaly, becomes positive (negative) during the westerly (easterly) shear due to the downdraft (updraft) associated with the meridional secondary circulation of the QBO (e.g., Plumb and Bell 1982). The temperature anomaly thereby provides useful information

as to the vertical transport of long-lived chemical species.

Before analyzing the PA run, we examined the effect of the different temporal averaging (monthly mean in the ST run and 1-day mean every three months in the PA run) on the QBO features in the zonal wind. Figure 3 shows the zonal wind anomalies obtained from the ST and PA runs at 1.4°N from 70 to 5 hPa between 1972 and 1990, together with zonal wind anomalies at 30 hPa, in which the anomalies of the PA run were calculated by subtracting an average value (over 18 years) for each calendar day present in the simulation. The 1-day mean data of the PA run certainly captures the QBO features of the stronger westerly shear as well as structures of strengths, durations, and periods, whereas fine temporal and vertical structures are unavoidably lost as stated before. Similarly, we examined the effect of the latitudinal width of the analyzed model data. It was confirmed that the QBO at one latitude at 1.4°N (Fig. 3a) resembles that of a latitudinal average within 10 degrees of the equator (Fig. 2c). Meanwhile the former exhibits a slightly larger amplitude than the latter as expected, as from the QBO amplitude of the zonal wind maximizes over the equator (e.g., Randel et al. 1999; Pascoe et al. 2005). These comparisons indicate that the 1-day zonal-mean data at three-month intervals at 1.4°N can
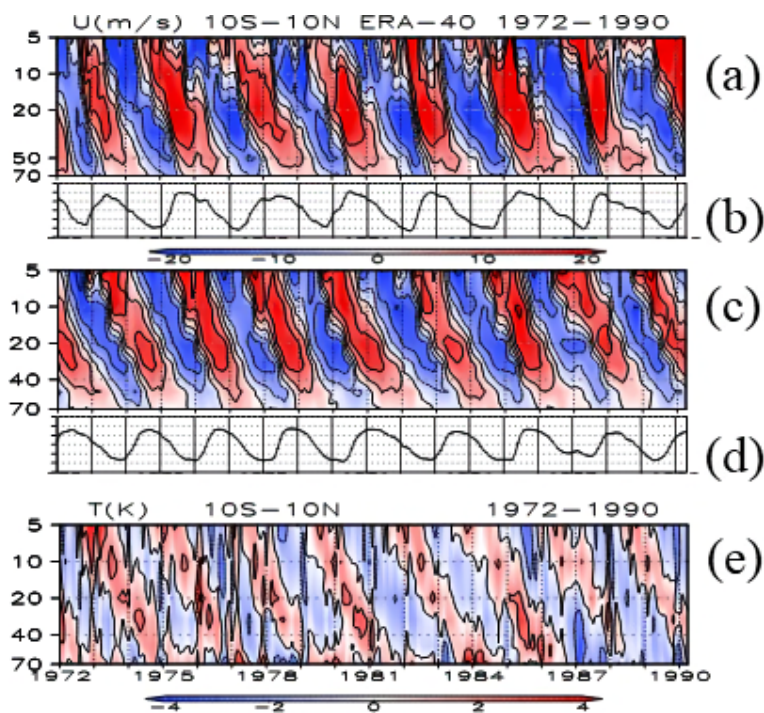
Fig. 2.   Time-pressure cross sections of zonal wind anomalies [m s^{-1}] averaged between 10°S and 10°N shown from 70 hPa to 5 hPa for 1972–1990 (a) in ERA-40, (c) in the ST run, and (e) temperature anomalies [K] in the ST run. Contour interval is 7 m s^{-1} for wind and 2 K for temperature. In addition, zonal wind anomalies (axis range: from −30 m s^{-1} to 30 m s^{-1}) at 30 hPa of (b) ERA-40 and (d) the ST run.
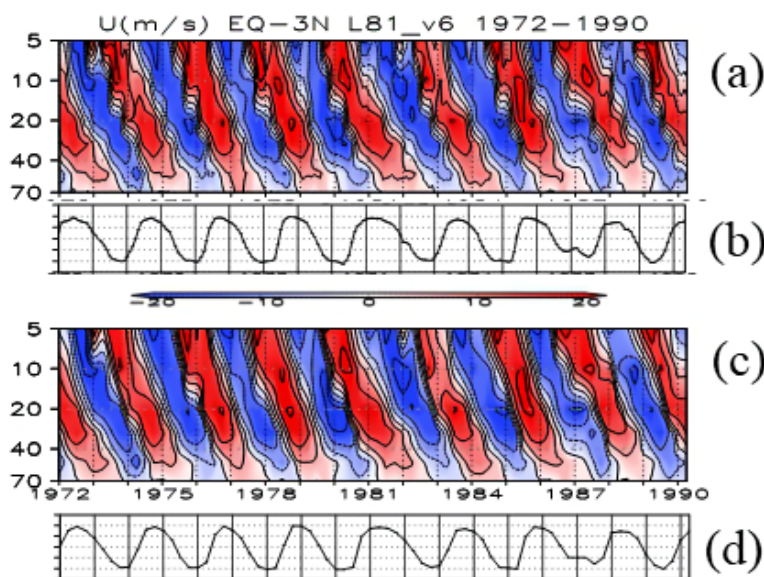
Fig. 3.   Time-pressure cross sections of zonal-mean zonal wind anomalies [m s^{-1}] at 1.4°N from 70 to 5 hPa for series of (a) monthly mean of the ST run and (c) 1-day mean at three-month intervals of the PA run, together with zonal wind anomalies (axis range: from −30 m s^{-1} to 30 m s^{-1}) at 30 hPa of (b) the ST run and (d) the PA run. Contour interval in (a) and (c) is 7 m s^{-1}.
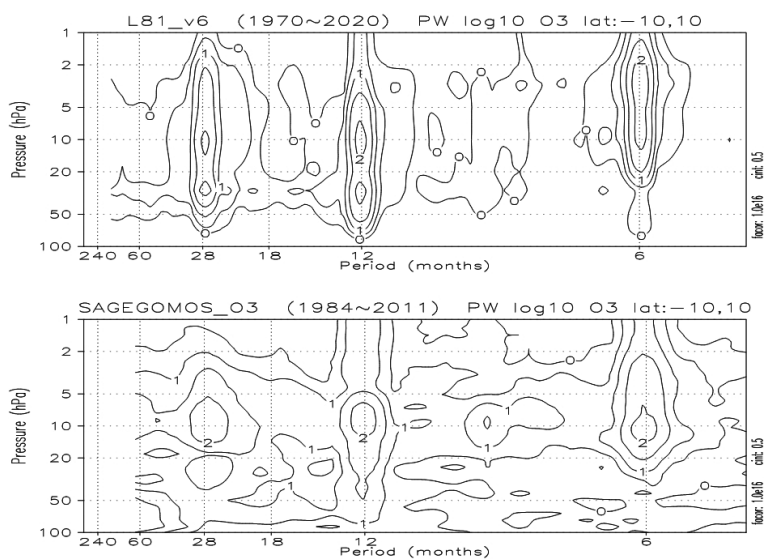
Fig. 4. Power spectrum of zonal-mean ozone from 100 hPa to 1 hPa averaged between 10°S and 10°N (upper) in the ST run from 1970 to 2020 and (lower) in the combined SAGE II-GOMOS ozone data from 1984 to 2011. Values are displayed in logarithmic scale of base 10, and units are $(10^{-2}$ ppmv$)^2$. Contour interval is 0.5.

be utilized for the analysis of the QBO in the tropics.

3.2 QBO in the chemistry fields of O_3 and NO_x

Figure 4 presents the power spectrum of the simulated and the observed zonal mean ozone mixing ratio, which is latitudinally averaged within 10 degrees of the equator from 100 to 1 hPa. The observation is based on the combined satellite data of SAGE II and GOMOS for 1984–2011 (Kyrölä et al. 2013), in which missing data of about a quarter of the entire period are filled through interpolation on the isobaric surface. Meanwhile in the power spectrum of the simulated and the observed ozone, three major modes of variability, the SAO, annual cycle, and the QBO, are apparent, although the altitudinal distribution of their variability is significantly different from that of the zonal-mean wind. The difference in the spectral distribution of SAO, annual cycle, and the QBO between ozone and wind is the same as in Kumar et al. (2011).

Figure 5 displays the time-pressure cross sections of the absolute and relative anomalies of O_3 and NO_x, which is averaged between 10°S and 10°N of the ST run from 70 hPa to 5 hPa in the year 1972–1990. Here, plots of NO_x instead of NO_2 (which is relevant for ozone loss, see Section 5.2.d) were presented, because NO_x is less affected by diurnal variations. NO_x is almost entirely composed of NO and NO_2 with a negligible contribution of NO_3, in particular below about 5 hPa (Liu et al. 2011). Almost all NO

is converted to NO_2 at night (e.g., Dessler 2000). On the other hand, at daytime, NO_2 is determined by NO_x and the partitioning within NO_x. However, since the variations of daily mean NO_2 are found to be closely related to those of the daily mean NO_x below about 10 hPa in the tropics, daily and monthly mean NO_x can serve as a proxy of NO_2 in this study, as in Park et al. (2017).

The ST run reproduces significant decreasing trend of O_3 in the upper stratosphere, which is about −1.3 % decade^{-1} at 10 hPa (not shown), being in quantitative agreement with satellite observations (e.g., World Meteorological Organization 2003). The decreasing trend of the upper stratospheric O_3 is attributed mainly to the increasing ClO_x, which stems from the increasing surface emissions of ODSs in the CCMVal-2 B2 scenario.

The model reproduces the phase transition of the ozone QBO from dynamical to photochemical control at around 28 km (~ 18 hPa) in observations by SAGE II (e.g., Zawodny and McCormick 1991; Chipperfield et al. 1994) and GOMOS (Hauchecorne et al. 2010), which results in a dogleg-shape pattern with a vertex slightly above 20 hPa in the ozone anomaly. The simulated maximum amplitude at around 30 hPa (~ 24 km) of about 10 % in relative value (anomaly divided by its climatology), from +0.6 ppmv to −0.4 ppmv in abundance range, below the phase transition, is slightly smaller than observations. The amplitude of about
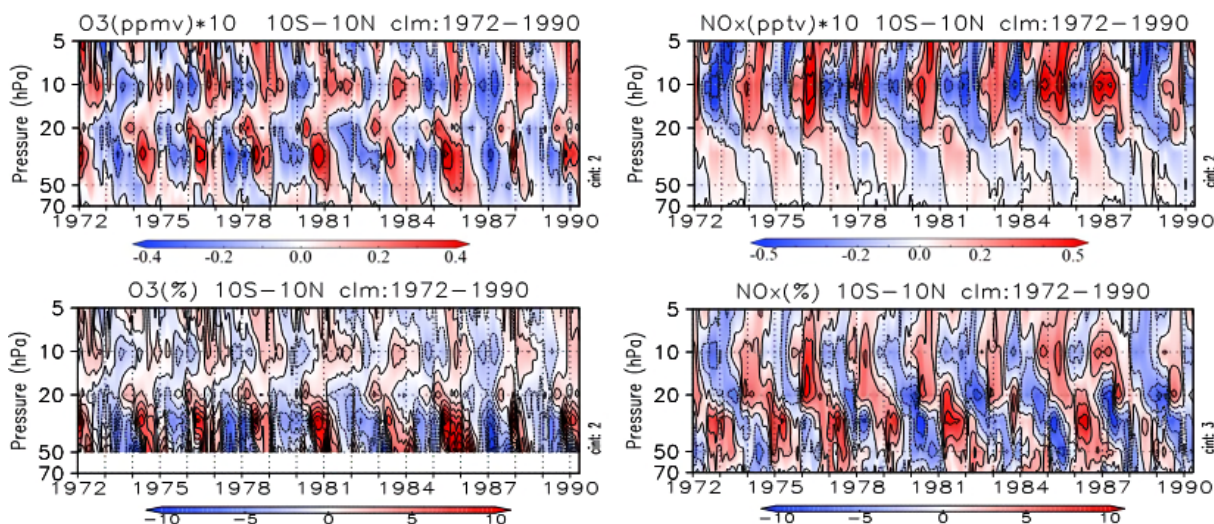
Fig. 5. Time-pressure cross sections of (left) O_3 and (right) NO_x (upper) absolute and (lower) relative anomalies. All data are detrended. Contour interval is 0.2 ppmv for absolute O_3, 2 % for relative O_3, 0.2 pptv for absolute NO_x, and 3 % for relative NO_x anomalies. Relative O_3 anomalies are not shown below 50 hPa, because they are out of scale.

4 % (~ 0.4 ppmv) at around 10 hPa (~ 31 km in the model) above the phase transition is quite identical to the observed values of about 5 % at 31 km (Zawodny and McCormick 1991; Chipperfield et al. 1994; Hauchecorne et al. 2010). While the O_3 amplitude below 50 hPa is small in absolute values, it is much larger in relative values (not shown due to out of scale) than that at 30 hPa, being consistent with the GOMOS data (Hauchecorne et al. 2010).

The absolute NO_x amplitude maximizes to about 0.7 pptv (~ 8 %) at 10 hPa. The relative amplitude is about 0.6 times of the observed values of about 13 % at 31 km (Zawodny and McCormick 1991; Chipperfield et al. 1994; Hauchecorne et al. 2010). In contrast to the ozone QBO, there is no phase reversal in the NO_x QBO, to allow the NO_x anomalies to propagate downward nearly continuously from the upper stratosphere like the temperature and wind anomalies. In addition, the absolute NO_x amplitude is smaller below 20 hPa, i.e., in the dynamically controlled altitudes, than that above 20 hPa. This is also in contrast to O_3, which shows substantial absolute amplitudes in both altitude regions.

4. Partitioning of ozone loss cycles in the QBO

Shown in Tables 1 and 2 are the PAP results for the significant catalytic cycles, contributing more than 99 % to the total ozone production and those contributing individually more than 2 % to the total ozone destruction at 10 hPa and 20 hPa. It entails that the

production cycles lead to the net reaction $3O_2 \rightarrow 2O_3$, and all the destruction cycles result in $2O_3 \rightarrow 3O_2$. Chapman reactions are said to the responsible in the ozone production in the entire vertical range except for the lowermost level at 70 hPa, where production due to the smog cycles (e.g., Grenfell et al. 2006) contributes about 4.4 % (not shown). In contrast to the production, the ozone destruction is seen to be more complicated and involves many cycles. The type (i.e., chemical species involved), order, and rates of the destruction cycles differ depending mainly on the altitude, and thus the partitioning among them varies from one altitude to another as shown in Tables 1 and 2.

In what follows, we are going to consider families of species and, correspondingly, families of cycles, to simplify the presentation of the results, include also the contribution of minor pathways not shown in Tables 1 and 2, and elucidate the role of different families of chemical species. We will assign a cycle to a family of species (NO_x, HO_x, ClO_x, BrO_x, or O_x) if at least one reaction in the cycle contains a reactant from this family. However, we will assign a cycle to the O_x family only if it contains a reaction between two O_x species such as $O + O_3 \rightarrow 2\,O_2$. Otherwise, all ozone loss cycles would be assigned to the O_x family, as they contain the reactant O_3. Moreover, the cycle (10-D2) is completely assigned to the NO_x family (like (10-D1)), although it contains the reaction $O(^1D) + N_2 \rightarrow O + N_2$ of the O_x species $O(^1D)$. This makes sense,

Table 1.   Daily and zonal mean ozone production and loss rates [ppbv day^{-1}] of major catalytic cycles at 10 hPa, 1.4°N, January 1, 1980. Numbers in parentheses represent the absolute ozone change rate due to the corresponding production or destruction cycles and the same value relative to the total production or destruction.

1.4°N, January 1, 1980, daily-mean

10 hPa, Production

O_2 + hv $\rightarrow$ O + O	(627 ppb day^{-1}, 99.9 %)	
2 × (O + O_2 + M $\rightarrow$ O_3 + M)		(10-P1)

10 hPa, Destruction

O_3 + hv $\rightarrow$ O + O_2 O + NO_2 $\rightarrow$ NO + O_2 O_3 + NO $\rightarrow$ NO_2 + O_2	(357 ppb day^{-1}, 54 %)	(10-D1)
O_3 + hv $\rightarrow$ O^{1}D + O_2 O^{1}D + N_2 $\rightarrow$ O + N_2 O + NO_2 $\rightarrow$ NO + O_2 O_3 + NO $\rightarrow$ NO_2 + O_2	(76 ppb day^{-1}, 12 %)	(10-D2)
O_3 + hv $\rightarrow$ O + O_2 O + O_3 $\rightarrow$ O_2 + O_2	(54 ppb day^{-1}, 8 %)	(10-D3)
O_3 + hv $\rightarrow$ O^{1}D + O_2 O^{1}D + O_2 $\rightarrow$ O + O_2 O + NO_2 $\rightarrow$ NO + O_2 O_3 + NO $\rightarrow$ NO_2 + O_2	(30 ppb day^{-1}, 5 %)	(10-D4)
O_3 + hv $\rightarrow$ O + O_2 ClO + O $\rightarrow$ Cl + O_2 Cl + O_3 $\rightarrow$ ClO + O_2	(30 ppb day^{-1}, 5 %)	(10-D5)
O_3 + hv $\rightarrow$ O + O_2 O + NO_2 $\rightarrow$ NO + O_2 ClO + NO $\rightarrow$ NO_2 + Cl Cl + O_3 $\rightarrow$ ClO + O_2	(25 ppb day^{-1}, 4 %)	(10-D6)
O_3 + hv $\rightarrow$ O + O_2 O + HO_2 $\rightarrow$ OH + O_2 OH + O_3 $\rightarrow$ HO_2 + O_2	(16 ppb day^{-1}, 2 %)	(10-D7)
O_3 + hv $\rightarrow$ O^{1}D + O_2 O^{1}D + N_2 $\rightarrow$ O + N_2 O + O_3 $\rightarrow$ O_2 + O_2	(12 ppb day^{-1}, 2 %)	(10-D8)

because the cycle (10-D2) is but identical to (10-D1), with the only difference in the O_3 photolysis channel (O_3 + hv $\rightarrow$ O(^{1}D) + O_2, O(^{1}D) + N_2 $\rightarrow$ O + N_2 is equivalent to O_3 + hv $\rightarrow$ O + O_2). The same argument applies to both (20-D5) and (20-D1). It is possible that a cycle is assigned to more than one family, e.g., (10-D6) to NO$_x$ and ClO$_x$. In this case, the rate of this cycle is divided by the number of these families, and the corresponding fraction of the rate is assigned to each family. For instance, half of the rate of cycle (10-D6) is assigned to NO$_x$ and the remaining half to ClO$_x$. By this assignment, the net role of each family can be determined through the summation of the contribution

of each cycle at a specific time and altitude. For example, at 10 hPa, ozone destruction due to NO$_x$-related cycles in Table 1 is about (357 + 76 + 30 + 0.5·25) ppbv day^{-1} ≈ 476 ppbv day^{-1}. However, for the final analysis, also cycles with small rates, not contained in Tables 1 and 2, will be taken into account.

Here we denote the monthly mean ozone loss rate due to the catalytic cycles of family "i" (NO$_x$, ClO$_x$, HO$_x$, O$_x$, or BrO$_x$) in month "l" (January, April, July, or October) in year "k" of total "N" years by δ^i_{kl}. Then, the climatological (annual mean) ozone loss rate will be calculated as $\delta^i_{clim} = (1/4N)\sum_{kl}\delta^i_{kl}$ for the cycles of family "i", which we also refer to simply as i-cycles

Table 2. The same as Table 1 except for 20 hPa.

1.4°N, January 1, 1980, daily-mean

20 hPa, Production

O_2	$+ hv$	$\rightarrow$	$O + O$	(109 ppb day^{-1}, 99.7 %)	
$2 \times (O$	$+ O_2$	$+ M$	$\rightarrow O_3 + M)$		(20-P1)

20 hPa, Destruction

O_3	$+ hv$	$\rightarrow O + O_2$	(43 ppb day^{-1}, 52 %)	
O	$+ NO_2$	$\rightarrow NO + O_2$		
O_3	$+ NO$	$\rightarrow NO_2 + O_2$		(20-D1)
O_3	$+ hv$	$\rightarrow O + O_2$	(10 ppb day^{-1}, 12 %)	
O	$+ O_3$	$\rightarrow O_2 + O_2$		(20-D2)
HO_2	$+ O_3$	$\rightarrow OH + 2O_2$	(7 ppb day^{-1}, 9 %)	
OH	$+ O_3$	$\rightarrow HO_2 + O_2$		(20-D3)
O_3	$+ hv$	$\rightarrow O + O_2$	(5 ppb day^{-1}, 6 %)	
ClO	$+ O$	$\rightarrow Cl + O_2$		
Cl	$+ O_3$	$\rightarrow ClO + O_2$		(20-D4)
O_3	$+ hv$	$\rightarrow O^1D + O_2$	(4 ppb day^{-1}, 5 %)	
O^1D	$+ N_2$	$\rightarrow O + N_2$		
O	$+ NO_2$	$\rightarrow NO + O_2$		
O_3	$+ NO$	$\rightarrow NO_2 + O_2$		(20-D5)
O_3	$+ hv$	$\rightarrow O + O_2$	(3 ppb day^{-1}, 3 %)	
O	$+ HO_2$	$\rightarrow OH + O_2$		
OH	$+ O_3$	$\rightarrow HO_2 + O_2$		(20-D6)
O_3	$+ hv$	$\rightarrow O + O_2$	(3 ppb day^{-1}, 3 %)	
O	$+ NO_2$	$\rightarrow NO + O_2$		
ClO	$+ NO$	$\rightarrow NO_2 + Cl$		
Cl	$+ O_3$	$\rightarrow ClO + O_2$		(20-D7)
O_3	$+ hv$	$\rightarrow O^1D + O_2$	(2 ppb day^{-1}, 2 %)	
O^1D	$+ O_2$	$\rightarrow O + O_2$		
O	$+ NO_2$	$\rightarrow NO + O_2$		
O_3	$+ NO$	$\rightarrow NO_2 + O_2$		(20-D8)

or cycles, omitting sometimes "family", henceforth. Further, the monthly mean ozone loss rate is $\delta^{sum}_{kl} = \sum_i \delta^i_{kl}$, and its climatological value is $\delta^{sum}_{clim} = (1/4N)\sum_{kl} \delta^{sum}_{kl}$. Figure 6 shows the climatological vertical profile of the (a) absolute (δ^i_{clim}) and (b) relative ($\delta^i_{clim}/\delta^{sum}_{clim}$) contribution of each family of cycles from 70 hPa to 5 hPa. The ozone loss rate expressed as change of mixing ratio per day [ppbv day^{-1}], simply referred to as ozone loss rate henceforth, increases nonlinearly with altitude for all the cycles, with NO$_x$ cycles accounting for the largest contribution in the entire vertical range. The contribution of other cycles differs, depending on altitude. For example, HO$_x$ cycles are the second-largest contributor below 20 hPa, but fourth at 10 hPa. On the other hand, O$_x$ and ClO$_x$ cycles, having much smaller rates than the HO$_x$ cycles below 50 hPa, reach a similar magnitude as the HO$_x$ cycles at 20 hPa and yield the second- and

third-largest contribution above 10 hPa. Meanwhile, the contribution of BrO$_x$ cycles is very small: less than a few percentages above 30 hPa and, at most, several percentages in the lowermost stratosphere below 70 hPa.

The absolute magnitude of each loss rate is about $10^{-2} \sim 10^{-1}$ ppbv day^{-1} at 70 hPa and 10^2 ppbv day^{-1} for ClO$_x$, HO$_x$, and O$_x$ cycles and 10^3 ppbv day^{-1} for NO$_x$ cycles at 10 hPa, and thus the magnitude ranges are about 10^4 from 70 hPa to 10 hPa. In contrast, BrO$_x$ cycles have a similar loss rate as the O$_x$ and ClO$_x$ cycles in the lower stratosphere, but the increase of their rate with altitude is much lesser compared to that of the other cycles, which results in the magnitude range of about 10^3. The relative magnitude, on the other hand, varies, depending on the altitude in certain ranges. NO$_x$ cycles contribute about 70 % at 10 hPa and about 60 % at other altitudes. HO$_x$ cycles con-
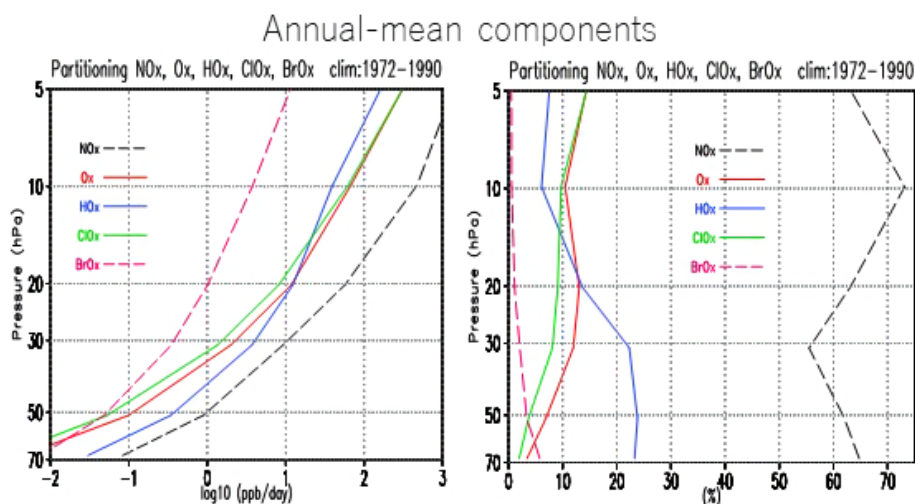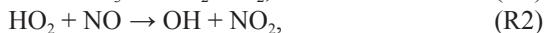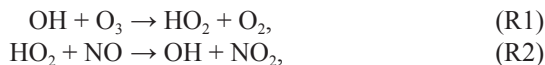
Fig. 6.　Vertical profiles of the annual mean ozone loss rate by NO_x, HO_x, ClO_x, O_x, and BrO_x catalytic cycles shown as (left) absolute values [ppbv day^{-1}] and (right) relative values [%] from 70 hPa to 5 hPa. Absolute values are displayed in logarithmic scale of base 10.

tribute slightly less than 10 % above 10 hPa and more than 20 % below 30 hPa, with an intermediate value of ~ 15 % at 20 hPa. O_x and ClO_x cycles are very close to each other within a few percentages, and they increase gradually with altitude from a few percentages at 70 hPa to ~ 15 % at 5 hPa.

These vertical profiles of loss rates are qualitatively similar to those in other off-line evaluations of chemistry (e.g., Osterman et al. 1997; Meul et al. 2014). But it is different in the lower stratosphere below 50 hPa, where HO_x cycles are considered to be the second-largest contributor (about 25 %) and the largest one. These said cycles contribute about 50 % at a northern mid-latitude site of 34.5°N in September according to Osterman et al. (1997), or about 80 % in the tropics averaged from 25°S to 25°N as per Meul et al. (2014). The discrepancy between the current results and those of Osterman et al. (1997) is at least partly caused by differences in season and location and in the abundances of chemical species: the simulated monthly zonal mean O_3, H_2O, and HO_2 abundances at 35°N at 50 hPa reach the minimum values around October. Still, these values are slightly larger than the annual mean abundances over the equator. A reason for the larger contribution of HO_x cycles in the study by Meul et al. (2014) is that they are splitting the zero cycle

$$OH + O_3 \rightarrow HO_2 + O_2, \tag{R1}$$
$$HO_2 + NO \rightarrow OH + NO_2, \tag{R2}$$

$$NO_2 + hv \rightarrow NO + O, \tag{R3}$$
$$O + O_2 + M \rightarrow O_3 + M, \tag{R4}$$

into O_3 production by reactions (R2)−(R4) and O_3 loss by reaction (R1), which adds more contribution to the HO_x cycles. Be that as it may, the partitioning of ozone loss in the lower stratosphere does not bring significant effects on the ozone mixing ratio, because the absolute values of the rates are very small. For instance, at 50 hPa, where the ozone mixing ratio is larger than 1 ppm, the loss rate is in the order of 1 ppb day^{-1} ~ 1 ppm (3 yr)$^{-1}$ (Fig. 6).

Figure 7 shows the time series of the deviation of the rate of each family of cycles from its mean value relative to the total climatological value [$(\delta^i_{kl} - \delta^i_{clim})/\delta^{sum}_{clim}$]. It also provides the corresponding quantity for the total loss rate [$(\delta^{sum}_{kl} - \delta^{sum}_{clim})/\delta^{sum}_{clim}$] from 1972 to 1990 for each altitude (10, 20, and 30 hPa) in the PA run, in which all quantities are detrended. In the un-detrended raw fields, the ClO_x cycles show a linearly increasing trend of about 5 % decade^{-1} at 10 hPa and a slight upward trend with very small QBO variations at 20 hPa and 30 hPa (not shown). It should be noted that with the deviations of the catalytic cycles not perfectly but partly synchronized, the NO_x relative loss rate deviation sometimes exceeds the sum of relative loss rates deviations (e.g., in January of 1980 and July of 1982 at 20 hPa).

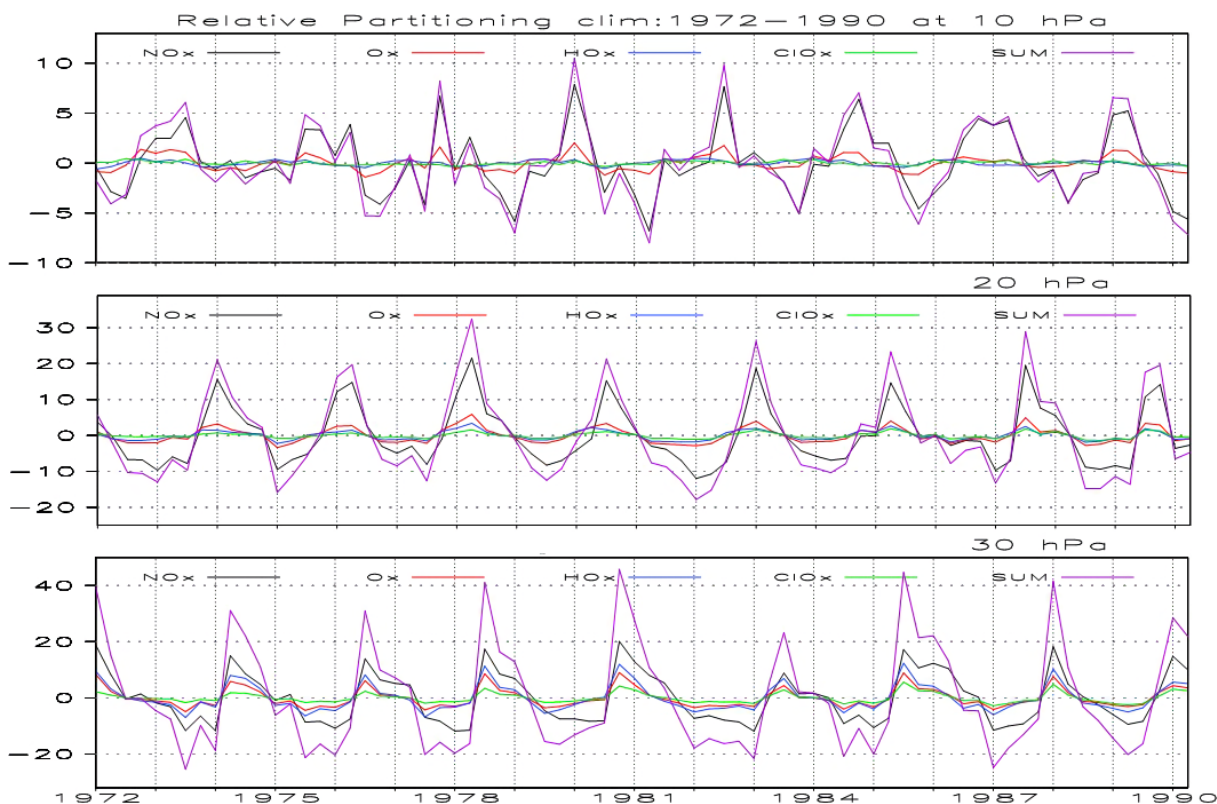The QBO components of the other cycles can be straightforwardly identified at each altitude, although

Fig. 7. Time series of the deviation of the rate of each family of catalytic cycles from the corresponding mean rate relative to the total climatological ozone loss rate $[(\delta^i_{kl} - \delta^i_{clim})/\delta^{sum}_{clim}]$ and the corresponding quantity for the total loss rate $[(\delta^{sum}_{kl} - \delta^{sum}_{clim})/\delta^{sum}_{clim}]$ at 10, 20, and 30 hPa from 1972 to 1990. All data are detrended.

positive components and negative components do not have symmetric shapes, particularly at 20 hPa and 30 hPa. The positive components are like triangle waves, while the negative components are like square waves at 20 hPa and 30 hPa. The QBO phase descending across altitudes can be easily detected, while QBO characteristics such as amplitude and phase duration differ from one QBO cycle to another. In addition, the correlation of the QBO amplitudes across altitudes differs from one descending QBO to another. For example, the positive peak of the total loss rate in the middle of 1980 at 20 hPa is smaller than the previous peak in 1978 and the following peak in 1983, while it is the largest of the three at 10 hPa and 30 hPa. To quantitatively obtain QBO components of the ozone loss rate, a Lanczos bandpass filter with cut-off periods of 15 months and 60 months (i.e., 5 unit and 20 unit lengths of three-month intervals) is applied to the ozone loss rates in the PA run (Fig. 7) over the entire time series of δ^i_{kl} from 1972 to 1990. After, the average QBO amplitude of each cycle ($A\delta^i_{QBO}$) is calculat-

ed as $\sqrt{2}\sigma$, where σ is the root mean square of the bandpass-filtered time series, by assuming a mono-chromatic wave. The same method is used for the sum of all cycles ($\delta^{sum}_{QBO} = \sum_i \delta^i_{QBO}$), so that the sum of the QBO amplitude of individual cycles is larger than the QBO amplitude of the sum of all cycles, $\sum_i A\delta^i_{QBO} > A\delta^{sum}_{QBO}$, because all the cycles are not completely in phase.

Figure 8 exhibits the vertical profile of the QBO amplitude of each family of cycles, presented as (a) absolute ($A\delta^i_{QBO}$) and (b) relative ($A\delta^i_{QBO}/A\delta^{sum}_{QBO}$) values. Since $\sum_i A\delta^i_{QBO} > A\delta^{sum}_{QBO}$ as stated above, the sum of the relative values exceeds 100 % by up to about 10 %. The absolute values of the QBO amplitudes are much smaller compared to those of the annual mean loss rates in Fig. 6. The QBO amplitude of the sum of all cycles amounts to about 4, 14, and 21 % of the annual mean of the total loss rate at 10, 20, and 30 hPa, respectively. The partitioning among the cycles, i.e., relative QBO amplitudes, more or less, resembles that of the annual mean for HO_x, ClO_x, and BrO_x
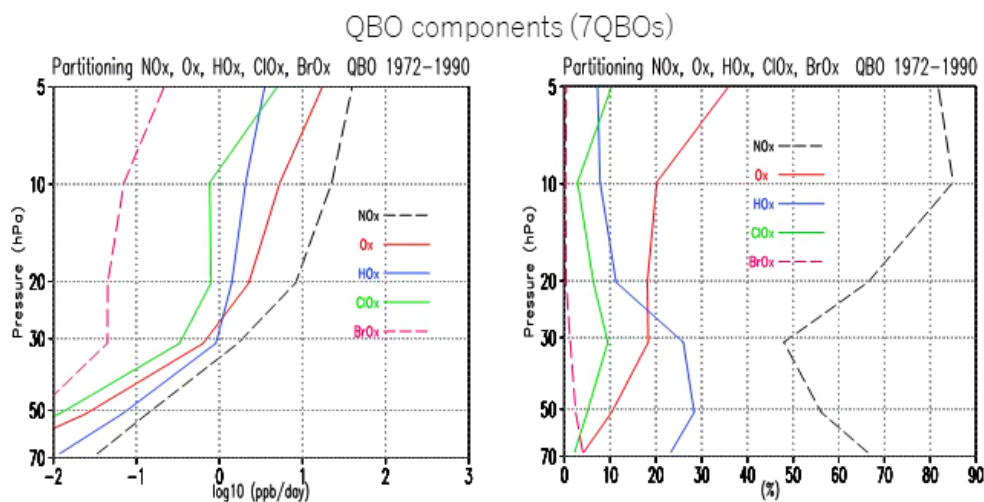
Fig. 8. Same as Fig. 6 except for the QBO amplitude.

cycles. However, NO_x and O_x cycles are substantially different. The contribution of NO_x cycles to the QBO of ozone loss is ~ 10 % smaller at 30 hPa and ~ 10 % larger at 10 hPa than the corresponding contribution to the annual mean ozone loss rate (shown in Fig. 6), whereas that of O_x cycles is several percentages larger at 50–10 hPa and 20 % larger at 5 hPa. Thus, the contribution of catalytic cycles to the QBO of the ozone loss rates can be summarized as follows: NO_x cycles have the largest fraction, which amounts to 50–85 % of the QBO amplitude of the total ozone loss rate. HO_x cycles account for the second-largest contribution (20–30 %) below 30 hPa and the third-largest contribution (about 10 %) above 20 hPa. Meanwhile, O_x cycles rank third (contributing 5–20 %) below 30 hPa and second (contributing about 20 %) above 20 hPa. For ClO_x cycles, they are in the fourth position with a nearly constant contribution of 5–10 %. Lastly, BrO_x cycles are almost negligible except below 50 hPa, contributing to around 3–5 %.

The ratio of the QBO amplitude of the two major catalytic cycles (O_x and NO_x), $A\delta^{Ox}_{QBO}/A\delta^{NOx}_{QBO}$, in the upper stratosphere is about 36 %/82 % ~ 0.44 at 5 hPa and about 20 %/85 % ~ 0.24 at 10 hPa. Tian et al. (2006) made a similar estimation using photochemical box model initialized with CCM output every 10 days over a 20-year simulation. They found that at 35 km (corresponding to 7 hPa in MRI-CCM), the QBO amplitude of O_x loss due to NO_x (reaction $NO_2 + O$) is ~ 2.8 % of the total O_x loss and that due to O_x is ~ 0.7 %. Hence, the corresponding ratio of the QBO amplitudes is $A\delta^{Ox}_{QBO}/A\delta^{NOx}_{QBO}$ ~ 0.7 %/2.8 % ~ 0.25,

which lies between the above-mentioned values of 0.24 (at 10 hPa) and 0.44 (at 5 hPa) in the present study.

5. Mechanism of the ozone QBO

To understand the regime change of the ozone QBO around 28 km, we investigated the dominant processes at two altitudes in more detail: 20 hPa (~ 26 km) in the dynamically controlled region and 10 hPa (~ 31 km) in the chemically controlled region. The ozone mixing ratio in the ascending branch of the Brewer-Dobson circulation, i.e., background ozone, is mainly determined by the combined action of vertical upward transport and chemical production and loss (resulting in chemical net ozone production in the lower stratosphere) during this ascent. Thereby, the ozone QBO, which is an anomaly component superimposed in the background ozone, is also governed by the combined action of vertical transport and chemistry.

5.1 Dynamically controlled region

At the dynamically controlled altitudes below 20 hPa, a consistent structure is maintained in the QBO between zonal wind, temperature, and chemical species through the secondary meridional circulation. In the westerly shear, i.e., during a strengthening of westerly zonal wind, there is a QBO-induced downdraft (Plumb and Bell 1982), which counteracts the background upward motion of the Brewer-Dobson circulation (Randel et al. 1999, Fig. 14; Fleming et al. 2002, Fig. 1). This QBO-induced downdraft induces adiabatic warming with cancelling radiative cooling.
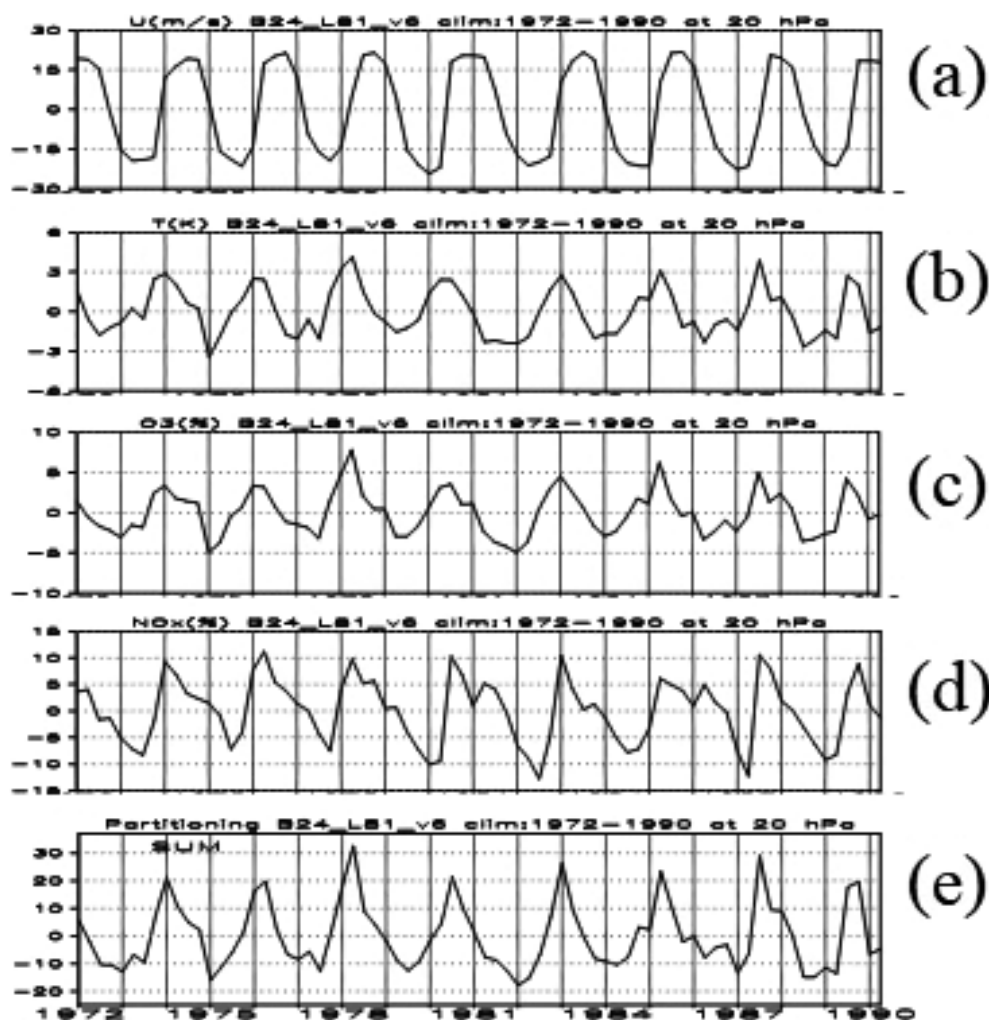
Fig. 9.   Time series of zonal-mean anomalies of (a) zonal wind [m s^{-1}], (b) temperature [K], (c) O$_3$ [%], (d) NO$_x$ [%], and (e) total ozone loss rate [%] at 20 hPa in the PA run.

Moreover, it has the effect that the vertical motion of air through the region of net ozone production (by O$_2$ photolysis) is slower, providing more time for ozone production in ascending air parcels and, thus, more ozone in this air. As there is net NO$_x$ production (from N$_2$O) in the lower stratosphere, arguments similar to those for O$_3$ also apply to NO$_x$. During easterly shear, the QBO generates an additional upward motion, changing the above argumentation to the opposite. These features are clearly shown in the non-filtered time series of zonal wind, temperature, O$_3$, NO$_x$, and ozone loss rate anomalies at 20 hPa (Fig. 9) in the PA run. Temperature precedes zonal wind by about a quarter cycle and is in phase with ozone.

Shibata and Deushi (2005b, Fig. 5) reproduced the phase relationships among wind, temperature, and ozone in three-dimensional model runs both with and without a feedback of ozone on temperature; this indicates that the feedback of ozone does not play a vital role on the phase relationship. Using the mechanistic one-dimensional model of Lin and London (1984), utilizing a simple linear damping term instead of a realistic chemical scheme, Hasebe (1994) concluded that the ozone solar heating feedback is key to reproduce this phase relation in the ozone QBO in the lower stratosphere. However, though not stated explicitly, the results of the study of Hasebe (1994, Figs. 6, 7) demonstrate that even the chemical effect alone can also reproduce a similar phase relation above 30 hPa, in agreement with a simulation with no feedback of
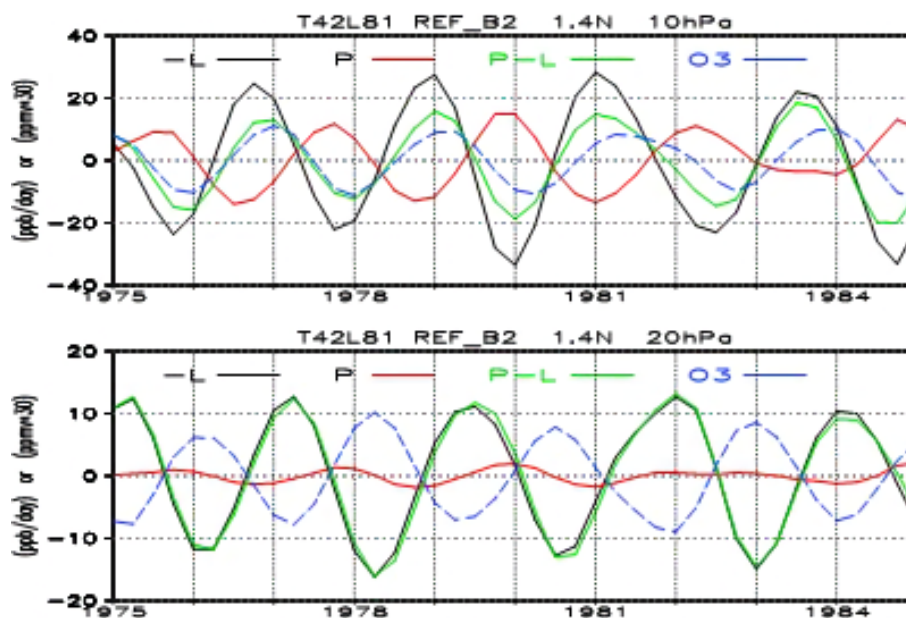
Fig. 10. Three-month interval series of the QBO ozone loss rate (-L, black), production rate (P, red), net production rate (P-L, green), and O_3 (dashed blue) at (upper) 10 hPa and (lower) 20 hPa in the PA run from 1975 to 1984. The QBO components are bandpass-filtered (15−60 months) data. Units are ppbv day^{-1} for loss rate and production rate and ppmv/30 for ozone.

ozone on temperature by Shibata and Deushi (2005b). There is still another potential mechanism for this phase relation. Bruhwiler and Hamilton (1999) demonstrated ozone horizontal transport by eddies to play a key role, at least in the vicinity of 40 hPa, through a GCM experiment with a non-interactive chemistry and nudged QBO forcing.

As the QBO amplitude of the ozone production is very small (Fig. 10, bottom), the variation of the net chemistry tendency (= production minus loss) of ozone is nearly identical to that of the loss rate alone (Fig. 10, bottom), so that, for investigating the role of chemistry, it is sufficient to consider only ozone loss. Figures 9 and 10 (bottom) show that the ozone loss rate (counted positive in the case of loss) is in phase with ozone; equivalently, the chemistry tendency is out of phase with ozone, similar to the results obtained at 30 hPa by Naoe et al. (2017). The phase relation among ozone, chemistry, transport, and net (addition of chemistry and transport) tendencies of the QBO components in the ST run is presented in Fig. 11. This phase relation demonstrates that the driving process of the ozone QBO at 20 hPa is not chemistry, but transport. The chemical ozone loss counteracts the ozone anomaly induced by transport and contributes to the phase shift of the ozone net tendency, which advances

ozone by a quarter cycle (Fig. 11).

The magnitude of the relative QBO amplitude of the ozone loss rate ($\approx$ 20 %) (Figs. 9e, 7, middle panel) may be roughly explained by the relative amplitudes of ozone ($\approx$ 5 %) and NO_x ($\approx$ 10 %) (Figs. 9c, d) and a contribution from the temperature variation of reaction rate constants (mainly K_{O+O2+M} of the reaction $O + O_2 + M \rightarrow O_3 + M$, affecting the ratio of the concentrations of atomic oxygen and ozone and K_{O+O3} of the reaction $O + O_3 \rightarrow 2 O_2$ in the O_x cycles).

5.2 Chemically controlled region

In the photochemically controlled altitudes above about 10 hPa, a dynamical structure similar to that at 20 hPa is still maintained between the QBO of zonal wind and temperature, with temperature preceding zonal wind by a quarter cycle as displayed in the time series at 10 hPa in the PA run (Fig. 12). The phase of NO_x lies between the phases of temperature and zonal wind. This slight advance of NO_x relative to the zonal wind at 20 hPa and 10 hPa is very similar to the feature of the lag-correlation between NO_2 and the zonal wind in SAGE II data (Hasebe 1994). The bandpass-filtered QBO time series in the ST run confirms that the phase relations between temperature and NO_x are identical to those at 20 hPa (not shown). However,
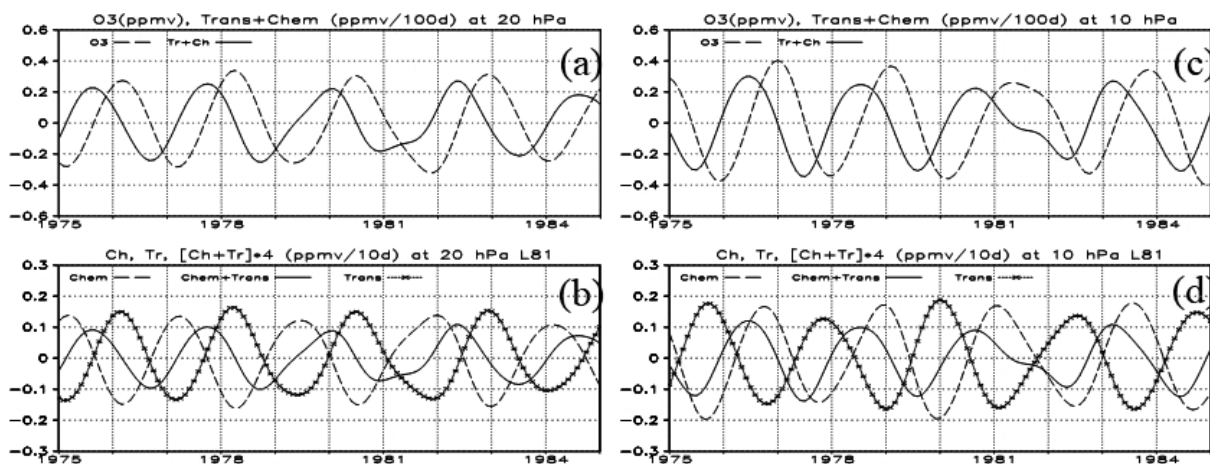
Fig. 11. QBO component time series of zonal and monthly mean ozone and its tendencies in the ST run from 1975 to 1985. (a) Ozone [ppmv] (dashed curve) and net tendency [ppmv $(100d)^{-1}$] (solid curve) at 20 hPa, (b) chemical (long-dashed), transport (dotted with crosses), and net (quadrupled, solid) tendencies [ppmv $(10d)^{-1}$] at 20 hPa. (c) The same as in (a) except for 10 hPa. (d) The same as in (b) except for 10 hPa.

ozone exhibits a different behavior. It is anti-correlated with temperature and zonal wind, so that the ozone maxima occur between temperature minima and zonal wind minima. Ozone is nearly out of phase with NO_x. The QBO amplitude of ozone at 10 hPa is $\approx 4\,\%$. In the next subsections, we are going to determine which factors contribute to this amplitude.

a. Ozone transport versus chemistry

The QBO amplitude of the temporal variation of ozone due to transport is ≈ 15 ppb day^{-1} (Fig. 11d). This is quite similar to the QBO amplitude of the ozone production rate as shown in Fig. 10 (upper panel). Consequently, both processes yield approximately equal contributions to the ozone variation. The relative contribution [%] of the ozone production, yielding a minor contribution to the ozone QBO, is discussed in more detail in Section 5.2.b.

The net production rate advances from ozone by about a 1/8 cycle (Fig. 10, upper panel). Ozone transport, on the other hand, is nearly out of phase to ozone in the bandpass-filtered QBO (Fig. 11d). This out of phase relation between transport and ozone indicates that transport does not drive the ozone QBO. Nevertheless, transport is but indispensable to make a phase advance of a quarter cycle for the net tendency against ozone. Accordingly, this phase relation among ozone, chemistry, and transport demonstrates that chemistry is a dominant driving force of the ozone QBO, although transport still plays a minor but significant role. This phase relation of chemistry to ozone at

10 hPa is in a sharp contrast to that in the dynamically controlled altitudes such as at 20 hPa (lower panel in Fig. 10), where chemistry (almost loss rate alone) and ozone are nearly out of phase as discussed in Section 5.1.

b. Chemistry: ozone production versus ozone loss

Since the production of ozone is attributed solely to Chapman reactions, involving the photolysis of O_2 (Table 1), an increase of the overhead ozone column immediately decreases the ozone production rate as solar ultraviolet irradiation is reduced, relevant for the photolysis rate coefficient J_{O_2} ($O_2 + h\nu \rightarrow O + O$), reaching 10 hPa. Analogously, a decrease of the overhead ozone column increases the ozone production. This would provide an explanation to the almost out of phase relation between the QBO components of the ozone production rate and the overhead column ozone (Fig. 13). The QBO amplitude of the O_3 production rate is slightly less than 2 % (Fig. 13). This is considerably smaller than the QBO amplitude of the ozone loss frequency, which is discussed in more detail in Section 5.2.c.

c. Chemical ozone loss: NO_x variations versus temperature variations

As was shown in Section 4, at 10 hPa, the NO_x cycles contribute about 85 % of the QBO amplitude of the ozone loss rate (Fig. 8), which is consistent with the results obtained by Ling and London (1986), Chipperfield et al. (1994), and Tian et al. (2006). That
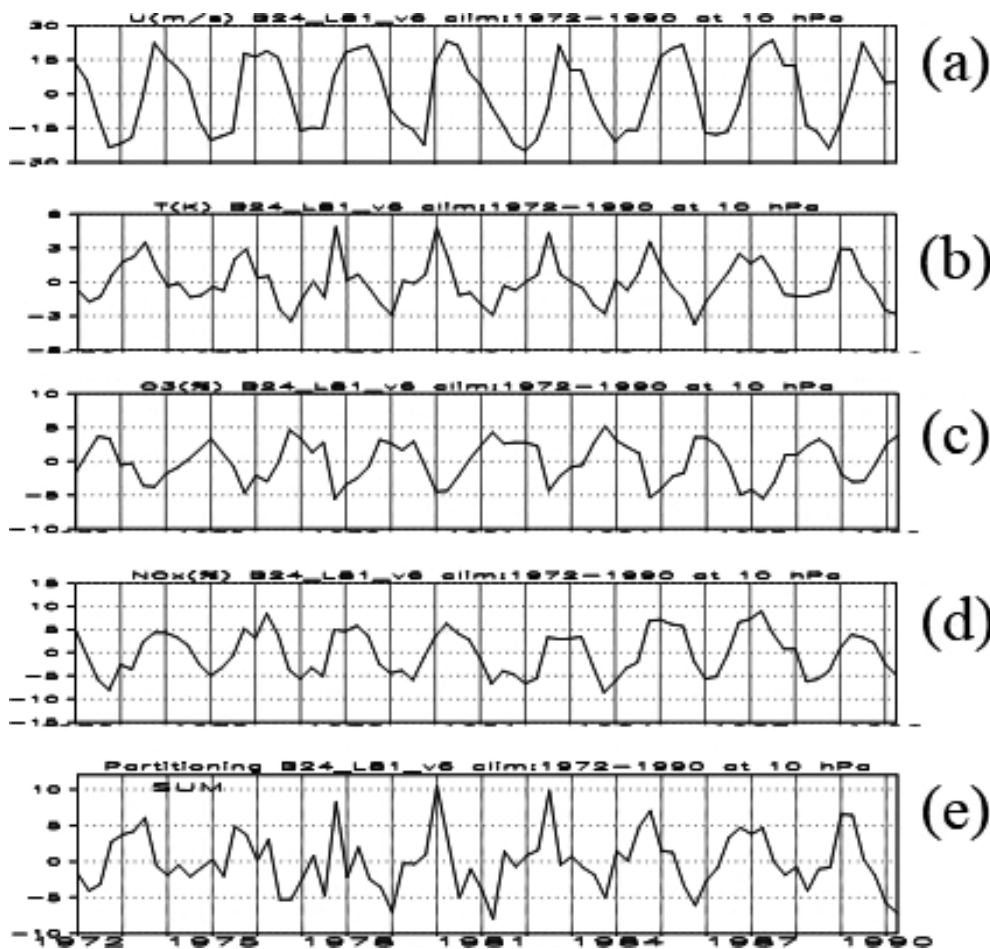
Fig. 12.   Time series of zonal mean anomalies of (a) zonal wind [m s^{-1}], (b) temperature [K], (c) O_3 [%], (d) NO_x [%], and (e) total ozone loss rate [%] at 10 hPa in the PA run.

is why we are going to investigate the causes of variations of the rate of the NO_x cycles in more detail in this subsection.

The rate-limiting reaction in the NO_x cycles shown in Table 1 is $O + NO_2 \rightarrow NO + O_2$ (with the rate constant K_{O+NO2}). The rate of this reaction is

$$K_{O+NO2} \cdot [O] \cdot [NO_2]$$
$$= K_{O+NO2} \cdot ([O]/[O_3]) \cdot ([NO_2]/[NO_x]) \cdot [NO_x] \cdot [O_3],$$
$$(1)$$

where [ ] denotes the concentration of a chemical species. Consequently, the reaction rate may be rewritten as $\Lambda_{O+NO2} \cdot [O_3]$, where Λ_{O+NO2} is the corresponding ozone loss frequency (Dessler 2000):
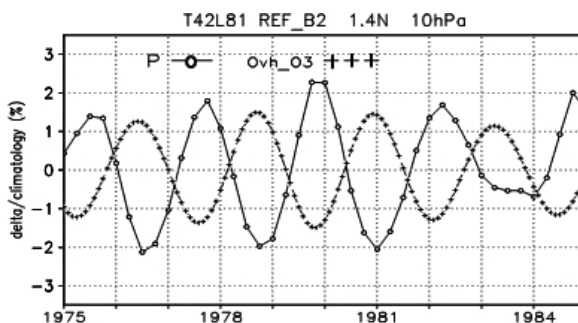

Fig. 13.   QBO component time series (at 10 hPa) of the daily mean ozone production rate [%] (solid curve with open circles) in the PA run and the monthly mean overhead column ozone [%] (dashed curve with plus signs) in the ST run. Both data are zonally averaged values.
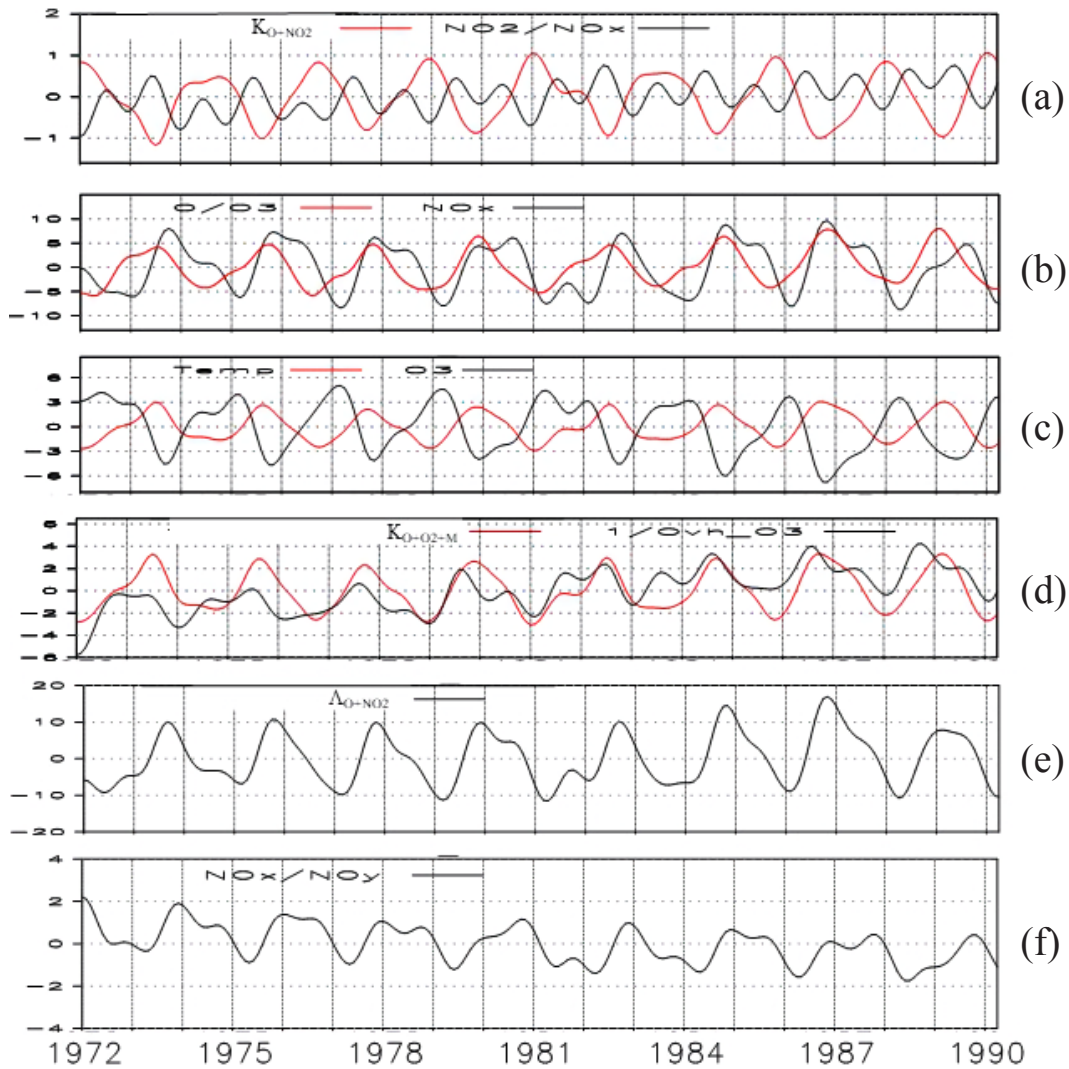
Fig. 14.   Time series of low-pass filtered anomalies of (a) K_{O+NO2} [%] (red curve) and $[NO_2]/[NO_x]$ [%] (black curve),
(b) $[O]/[O_3]$ [%] (red curve) and NO_x [%] (black curve), (c) temperature [K] (red curve) and O_3 [%] (black curve),
(d) $1/K_{O+O2+M}$ [%] (red curve) and $1/(over\_head\_O_3)$ [%] (black curve), and (e) $\varLambda_{O+NO2}$ [%], and (f) $[NO_x]/[NO_y]$ [%]
at 10 hPa in the ST run. All data are zonally and monthly averaged values. The cut-off period is 10 months.

$$\varLambda_{O+NO2} = K_{O+NO2} \cdot ([O]/[O_3]) \cdot ([NO_2]/[NO_x]) \cdot [NO_x]. \tag{2}$$

As the NO_x cycles destroy two ozone molecules, the corresponding ozone loss rate is $2 \cdot \varLambda_{O+NO2} \cdot [O_3]$. The time series of anomalies of $\varLambda_{O+NO2}$ is shown in Fig. 14e. It has an amplitude of ≈ 10 %.

As shown in Eqs. (1) and (2), the ozone loss frequency is dependent on four factors: K_{O+NO2}, $[O]/[O_3]$, $[NO_2]/[NO_x]$, and $[NO_x]$. We investigate how these quantities are modulated by the QBO of temperature and $[NO_x]$:

a) K_{O+NO2} depends slightly on temperature, being negatively correlated with it. Its QBO amplitude is about 1 % (Fig. 14a).

b) $[O]/[O_3]$ has a QBO amplitude of ≈ 5 %. It is determined by the equilibrium of the O production by ozone photolysis and the O loss by the reaction $O + O_2 + M \rightarrow O_3 + M$. The ozone photolysis frequency mostly depends on the overhead ozone column, as it has a decreasing trend and a QBO amplitude of ≈ 2 % (Fig. 14d). Meanwhile, the rate constant K_{O+O2+M} of the three-body reaction $O + O_2 + M \rightarrow O_3 + M$ depends significantly on tempera-

ture: a higher temperature would result in a smaller K_{O+O2+M}. Consequently, $1/K_{O+O2+M}$ is in phase with temperature (Figs. 14c, d). Its QBO amplitude is $\approx$ 3 % (Fig. 14d).

c) The QBO amplitude of $[NO_2]/[NO_x]$ is approximately smaller than 0.8 % (Fig. 14a). This means that the chemical repartitioning within the NO_x family does not significantly affect the ozone QBO.

d) The QBO amplitude of $[NO_x]$ is $\approx$ 8 % (Fig. 14b). Consequently, the NO_x variation brings the largest contribution to the ozone QBO, and temperature is also a significant driver with its temperature dependence of $[O]/[O_3]$.

d. NO_x variations: NO_y transport versus chemistry

Finally, we will look into the reason for the NO_x variations mentioned in the previous subsection. They might arise from different amounts of NO_y ($= N + NO + NO_2 + NO_3 + 2N_2O_5 + HNO_3 + HO_2NO_2 + ClONO_2 + ClNO_2 + BrONO_2$) being transported to the altitude of interest or from a chemical repartitioning within the NO_y family. Figure 14f shows the time series of $[NO_x]/[NO_y]$, which has a QBO amplitude of $\approx$ 1 %. As this is significantly smaller than the amplitude of $[NO_x]$ ($\approx$ 8 %, cf. Fig. 14b), the effect of the repartitioning of NO_y by chemical reactions is relatively small. Consequently, the main contribution to the NO_x variation originates in the variation of NO_y transport. However, a detailed analysis of the transport of NO_x and NO_y still needs further work, because in the simulation, most species were stored not in daily but in monthly intervals, except for O_3, HF, and N_2O.

6. Conclusions

The ozone QBO in the tropical stratosphere simulated by MRI-CTM (T42L81) was investigated to quantify the partitioning of the ozone loss rate among the significant catalytic cycles due to NO_x, HO_x, ClO_x, O_x, and BrO_x. The PAP, developed by Lehmann (2004, 2002), was used. Detailed chemistry data required for PAP was prepared at a specific latitude (1.4°N), which is nearest to the equator in T42 resolution. It entails making 1-day simulations at three-month intervals (January, April, July, and October) for a span of 18 years. This started in 1972 using the restart data of the standard simulation by the same CTM under realistic climate forcings of time-evolving GHGs, ODSs, and SST with fixed solar minimum and background aerosol conditions in the stratosphere, i.e., CCMVal-2 B2 scenario (SPARC CCMVal 2010). The 1-day simulations at three-month intervals reproduced the overall features of the QBO in the standard simulation.

The absolute values of the QBO amplitudes of the catalytic cycles are much smaller than the annual mean ozone loss rate. The QBO amplitude of the sum of all cycles is about 4, 14, and 21 % of the annual mean of the total loss rate at 10, 20, and 30 hPa, respectively. NO_x cycles contribute the largest fraction to the QBO amplitude of the ozone loss rate (50−85 %, depending on altitude). On the other hand, HO_x cycles account for the second-largest contribution (20−30 %) below 30 hPa and the third-largest contribution (about 10 %) above 20 hPa. Meanwhile, O_x cycles rank third (contributing 5−20 %) below 30 hPa and second (contributing about 20 %) above 20 hPa. ClO_x cycles are in the fourth position with a nearly constant contribution of 5−10 %. Last but not the least, BrO_x cycles ranked the lowest, as they are almost negligible except below 50 hPa. While the order of these cycles in the QBO is the same as the order of their contribution to the annual mean ozone loss rate, the magnitude of their contribution is different, in particular for NO_x and O_x cycles, where a difference of up to about 10 % (for NO_x cycles) or 20 % (for O_x cycles) exists.

In the dynamically controlled region below 20 hPa, the phase analysis among ozone, transport, and chemistry confirmed that transport is a major driver of the ozone QBO and that chemistry has a significant role to play to make the net tendency advance a quarter cycle against ozone. At 10 hPa, i.e., in the photochemically controlled region, the NO_x cycles are found to contribute about 85 % to the QBO amplitude of the ozone loss rate. The rate-limiting reaction in the NO_x cycles, $O + NO_2 \rightarrow NO + O_2$ (rate constant K_{O+NO2}), leads to the ozone loss frequency (pseudo first-order rate constant) as a product of four quantities,

$$\Lambda_{O+NO2} = K_{O+NO2}([O]/[O_3]) \cdot ([NO_2]/[NO_x]) \cdot [NO_x].$$

Out of these four, the contributions from K_{O+NO2} and $[NO_2]/[NO_x]$ to the QBO amplitude of Λ_{O+NO2} are very small (about 1 %). The QBO amplitudes of $[NO_x]$ and $[O]/[O_3]$ are about 8 % and 5 % of the mean values of $[NO_x]$ and $[O]/[O_3]$. The ratio $[O]/[O_3]$ is determined by the equilibrium of the O production by oxygen photolysis and the O loss by the three-body reaction $O + O_2 + M \rightarrow O_3 + M$. The rate constant of this reaction depends strongly on temperature. Consequently, $[NO_x]$ is a major contributor to the QBO amplitude of the ozone loss rate in the photochemically controlled region at 10 hPa, and temperature is the second most important contributor through the temperature dependence of $[O]/[O_3]$. Minor contributions emerge from the QBO variation of the overhead ozone column, which modulates the ozone photolysis, influencing

[O]/[O$_3$], and the oxygen photolysis, leading to O$_3$ production.

References

Baldwin, M. P., L. J. Gray, T. J. Dunkerton, K. Hamilton, P. H. Haynes, W. J. Randel, J. R. Holton, M. J. Alexander, I. Hirota, T. Horinouchi, D. B. A. Jones, J. S. Kinnersley, C. Marquardt, K. Sato, and M. Takahashi, 2001: The quasi-biennial oscillation. *Rev. Geophys.*, **39**, 179–229.

Bruhwiler, L. P., and K. Hamilton, 1999: A numerical simulation of the stratospheric ozone quasi-biennial oscillation using a comprehensive general circulation model. *J. Geophys. Res.*, **104**, 30525–30557.

Butchart, N., A. A. Scaife, J. Austin, S. H. E. Hare, and J. R. Knight, 2003: Quasi-biennial oscillation in ozone in a coupled chemistry-climate model. *J. Geophys. Res.*, **108**, 4486, doi:10.1029/2002JD003004.

Chipperfield, M. P., L. J. Gray, J. S. Kinnersley, and J. Zawodny, 1994: A two-dimensional model study of the QBO signal in SAGE II NO$_2$ and O$_3$. *Geophys. Res. Lett.*, **21**, 589–592.

Dee, D. P., S. M. Uppala, A. J. Simmons, P. Berrisford, P. Poli, S. Kobayashi, U. Andrae, M. A. Balmaseda, G. Balsamo, P. Bauer, P. Bechtold, A. C. M. Beljaars, L. van de Berg, J. Bidlot, N. Bormann, C. Delsol, R. Dragani, M. Fuentes, A. J. Geer, L. Haimberger, S. B. Healy, H. Hersbach, E. V. Hólm, L. Isaksen, P. Kållberg, M. Köhler, M. Matricardi, A. P. McNally, B. M. Monge-Sanz, J.-J. Morcrette, B.-K. Park, C. Peubey, P. de Rosnay, C. Tavolato, J.-N. Thépaut, and F. Vitart, 2011: The ERA-Interim reanalysis: Configuration and performance of the data assimilation system. *Quart. J. Roy. Meteor. Soc.*, **137**, 553–597.

Dessler, A. E., 2000: *The Chemistry and Physics of Stratospheric Ozone*. Academic Press, 214 pp.

Fleming, E. L., C. H. Jackman, J. E. Rosenfield, and D. B. Considine, 2002: Two-dimensional model simulations of the QBO in ozone and tracers in the tropical stratosphere. *J. Geophys. Res.*, **107**, 4665, doi:10.1029/2001JD001146.

Grenfell, J. L., R. Lehmann, P. Mieth, U. Langematz, and B. Steil, 2006: Chemical reaction pathways affecting stratospheric and mesospheric ozone. *J. Geophys. Res.*, **111**, D17311, doi:10.1029/2004JD005713.

Grenfell, J. L., S. Gebauer, M. Godolt, K. Palczynski, H. Rauer, J. Stock, P. von Paris, R. Lehmann, and F. Selsis, 2013: Potential biosignatures in super-Earth atmospheres. II. Photochemical responses. *Astrobiol-ogy*, **13**, 415–438.

Hasebe, F., 1994: Quasi-biennial oscillations of ozone and diabatic circulation in the equatorial stratosphere. *J. Atmos. Sci.*, **51**, 729–745.

Hauchecorne, A., J. L. Bertaux, F. Dalaudier, P. Keckhut, P. Lemennais, S. Bekki, M. Marchand, J. C. Lebrun, E. Kyrölä, J. Tamminen, V. Sofieva, D. Fussen, F. Vanhellemont, O. Fanton d'Andon, G. Barrot, L. Blanot, T. Fehr, and L. Saavedra de Miguel, 2010: Response of tropical stratospheric O$_3$, NO$_2$ and NO$_3$ to the equatorial Quasi-Biennial Oscillation and to temperature as seen from GOMOS/ENVISAT. *Atmos. Chem. Phys.*, **10**, 8873–8879.

Hines, C. O., 1997: Doppler-spread parameterization of gravity-wave momentum deposition in the middle atmosphere. Part 2: Broad and quasi monochromatic spectra, and implementation. *J. Atmos. Sol.-Terr. Phys.*, **59**, 387–400.

Jucks, K. W., D. G. Johnson, K. V. Chance, W. A. Traub, R. J. Salawitch, and R. A. Stachnik, 1996: Ozone production and loss rate measurements in the middle stratosphere. *J. Geophys. Res.*, **101**, 28785–28792.

Kumar, K. K., D. Swain, S. R. John, and G. Ramkumar, 2011: Simultaneous observations of SAO and QBO in winds, temperature and ozone in the tropical middle atmosphere over Thumba (8.5°N, 77°E). *Climate Dyn.*, **37**, 1961–1973.

Kyrölä, E., M. Laine, V. Sofieva, J. Tamminen, S.-M. Päivärinta, S. Tukiainen, J. Zawodny, and L. Thomason, 2013: Combined SAGE II–GOMOS ozone profile data set for 1984–2011 and trend analysis of the vertical distribution of ozone. *Atmos. Chem. Phys.*, **13**, 10645–10658.

Lehmann, R., 2002: Determination of dominant pathways in chemical reaction systems: An algorithm and its application to stratospheric chemistry. *J. Atmos. Chem.*, **41**, 297–314.

Lehmann, R., 2004: An algorithm for the determination of all significant pathways in chemical reaction systems. *J. Atmos. Chem.*, **47**, 45–78.

Ling, X.-D., and J. London, 1986: The quasi-biennial oscillation of ozone in the tropical middle stratosphere: A one-dimensional model. *J. Atmos. Sci.*, **43**, 3122–3137.

Liu, Y., C. H. Lu, Y. Wang, and E. Kyrölä, 2011: The quasi-biennial and semi-annual oscillation features of tropical O$_3$, NO$_2$, and NO$_3$ revealed by GOMOS satellite observations for 2002–2008. *Chin. Sci. Bull.*, **56**, 1921–1929.

Meul, S., U. Langematz, S. Oberländer, H. Garny, and P. Jöckel, 2014: Chemical contribution to future tropical ozone change in the lower stratosphere. *Atmos. Chem. Phys.*, **14**, 2959–2971.

Müller, R., J.-U. Grooß, A. M. Zafar, S. Robrecht, and R. Lehmann, 2018: The maintenance of elevated active chlorine levels in the Antarctic lower stratosphere

through HCl null cycles. *Atmos. Chem. Phys.*, **18**, 2985–2997.

Naoe, H., and K. Shibata, 2010: Equatorial quasi-biennial oscillation influence on northern winter extratropical circulation. *J. Geophys. Res.*, **115**, D19102, doi: 10.1029/2009JD012952.

Naoe, H., M. Deushi, K. Yoshida, and K. Shibata, 2017: Future changes in the ozone quasi-biennial oscillation with increasing GHGs and ozone recovery in CCMI simulations. *J. Climate*, **30**, 6977–6997.

Nevison, C. D., S. Solomon, and R. S. Gao, 1999: Buffering interactions in the modeled response of stratospheric O_3 to increased NO_x and HO_x. *J. Geophys. Res.*, **104**, 3741–3754.

Osterman, G. B., R. J. Salawitch, B. Sen, G. C. Toon, R. A. Stachnik, H. M. Pickett, J. J. Margitan, J.-F. Blavier, and D. B. Peterson, 1997: Balloon-borne measurements of stratospheric radicals and their precursors: Implications for the production and loss of ozone. *Geophys. Res. Lett.*, **24**, 1107–1110.

Park, M., W. J. Randel, D. E. Kinnison, A. E. Bourassa, D. A. Degenstein, C. Z. Roth, C. A. McLinden, C. E. Sioris, N. J. Livesey, and M. L. Santee, 2017: Variability of stratospheric reactive nitrogen and ozone related to the QBO. *J. Geophys. Res.: Atmos.*, **122**, 10103–10118.

Pascoe, C. L., L. J. Gray, S. A. Crooks, M. N. Juckes, and M. P. Baldwin, 2005: The quasi-biennial oscillation: Analysis using ERA-40 data. *J. Geophys. Res.*, **110**, D08105, doi:10.1029/2004JD004941.

Plumb, R. A., and R. C. Bell, 1982: A model of the quasi-biennial oscillation on an equatorial beta-plane. *Quart. J. Roy. Meteor. Soc.*, **108**, 335–352.

Randel, W. J., F. Wu, R. Swinbank, J. Nash, and A. O'Neill, 1999: Global QBO circulation derived from UKMO stratospheric analyses. *J. Atmos. Sci.*, **56**, 457–474.

Sander, S. P., B. J. Finlayson-Pitts, R. R. Friedl, D. M. Golden, R. E. Huie, C. E. Kolb, M. J. Kurylo, M. J. Molina, G. K. Moortgat, V. L. Orkin, and A. R. Ravishankara, 2002: *Chemical kinetics and photochemical data for use in atmospheric studies, Evaluation Number 14*. JPL Publication 02-25, Jet Propulsion Laboratory.

Sander, S. P., B. J. Finlayson-Pitts, R. R. Friedl, D. M. Golden, R. E. Huie, H. Keller-Rudek, C. E. Kolb, M. J. Kurylo, M. J. Molina, G. K. Moortgat, V. L. Orkin, A. R. Ravishankara, and P. H. Wine, 2006: *Chemical kinetics and photochemical data for use in atmospheric studies, Evaluation Number 15*. JPL Publication 06-2, Jet Propulsion Laboratory.

Shibata, K., and M. Deushi, 2005a: Partitioning between resolved wave forcing and unresolved gravity wave forcing to the quasi-biennial oscillation as revealed with a coupled chemistry-climate model. *Geophys. Res. Lett.*, **32**, L12820, doi:10.1029/2005GL022885.

Shibata, K., and M. Deushi, 2005b: Radiative effect of ozone on the quasi-biennial oscillation in the equa-torial stratosphere. *Geophys. Res. Lett.*, **32**, L24802, doi:10.1029/ 2005GL023433.

Shibata, K., and M. Deushi, 2008a: *Simulation of the stratospheric circulation and ozone during the recent past (1980–2004) with the MRI chemistry-climate model*. CGER's Supercomputer Monograph Report Vol.13, National Institute for Environmental Studies, Japan, 154 pp.

Shibata, K., and M. Deushi, 2008b: Long-term variations and trends in the simulation of the middle atmosphere 1980–2004 by the chemistry-climate model of the Meteorological Research Institute. *Ann. Geophys.*, **26**, 1299–1326.

Shibata, K., and M. Deushi, 2012: Future changes in the quasi-biennial oscillation under a greenhouse gas increase and ozone recovery in transient simulations by a chemistry-climate model. *Greenhouse Gases - Emission, Measurement and Management*. Liu, G. (ed.), InTech, 355–386.

Stock, J. W., C. S. Boxe, R. Lehmann, J. L. Grenfell, A. B. C. Patzer, H. Rauer, and Y. L. Yung, 2012a: Chemical pathway analysis of the Martian atmosphere: CO_2-formation pathways. *Icarus*, **219**, 13–24.

Stock, J. W., J. L. Grenfell, R. Lehmann, A. B. C. Patzer, and H. Rauer, 2012b: Chemical pathway analysis of the lower Martian atmosphere: The CO_2 stability problem. *Planet. Space Sci.*, **68**, 18–24.

Stock, J. W., C. S. Blaszczak-Boxe, R. Lehmann, J. L. Grenfell, A. B. C. Patzer, H. Rauer, and Y. L. Yung, 2017: A detailed pathway analysis of the chemical reaction system generating the Martian vertical ozone profile. *Icarus*, **291**, 192–202.

SPARC CCMVal, 2010: *SPARC CCMVal report on the evaluation of chemistry-climate models*. Eyring, V., T. G. Shepherd, and D. W. Waugh (eds.), SPARC Report No. 5, WCRP-132, WMO/TD-No. 1526, SPARC.

Tian, W., M. P. Chipperfield, L. J. Gray, and J. M. Zawodny, 2006: Quasi-biennial oscillation and tracer distributions in a coupled chemistry-climate model. *J. Geophys. Res.*, **111**, D20301, doi:10.1029/2005JD006871.

Uppala, S. M., P. W. Kållberg, A. J. Simmons, U. Andrae, V. da Costa Bechtold, M. Fiorino, J. K. Gibson, J. Haseler, A. Hernandez, G. A. Kelly, X. Li, K. Onogi, S. Saarinen, N. Sokka, R. P. Allan, E. Andersson, K. Arpe, M. A. Balmaseda, A. C. M. Beljaars, L. van de Berg, J. Bidlot, N. Bormann, S. Caires, F. Chevallier, A. Dethof, M. Dragosavac, M. Fisher, M. Fuentes, S. Hagemann, E. Hólm, B. J. Hoskins, L. Isaksen, P. A. E. M. Janssen, R. Jenne, A. P. McNally, J.-F. Mahfouf, J.-J. Morcrette, N. A. Rayner, R. W. Saunders, P. Simon, A. Sterl, K. E. Trenberth, A. Untch, D. Vasiljevic, P. Viterbo, and J. Woollen, 2005: The ERA-40 Reanalysis. *Quart. J. Roy. Meteor. Soc.*, **131**, 2961–3012.

Verronen, P. T., and R. Lehmann, 2013: Analysis and parameterisation of ionic reactions affecting middle atmo-

spheric HO_x and NO_y during solar proton events. *Ann. Geophys.*, **31**, 909–956.

Verronen, P. T., M. L. Santee, G. L. Manney, R. Lehmann, S.-M. Salmi, and A. Seppälä, 2011: Nitric acid enhancements in the mesosphere during the January 2005 and December 2006 solar proton events. *J. Geophys. Res.*, **116**, D17301, doi:10.1029/2011JD016075.

Wennberg, P. O., R. C. Cohen, R. M. Stimpfle, J. P. Koplow, J. G. Anderson, R. J. Salawitch, D. W. Fahey, E. L. Woodbridge, E. R. Keim, R. S. Gao, C. R. Webster, R. D. May, D. W. Toohey, L. M. Avallone, M. H. Proffitt, M. Loewenstein, J. R. Podolske, K. R. Chan, and S. C.

Wofsy, 1994: Removal of stratospheric O_3 by radicals: In situ measurements of OH, HO_2, NO, NO_2, ClO, and BrO. *Science*, **266**, 398–404.

World Meteorological Organization, 2003: *Scientific assessment of ozone depletion: 2002, global ozone research and monitoring project*. Report No. 47, World Meteorological Organization, Geneva.

Zawodny, J. M., and M. P. McCormick, 1991: Stratospheric aerosol and gas experiment II: Measurements of the quasi-biennial oscillation in ozone and nitrogen dioxide. *J. Geophys. Res.*, **96**, 9371–9377.